Influence of the surface energy of a basalt fiber on capillary wicking and in-plane permeability of reinforcements

Romain Ravel, Monica Francesca Pucci, Pierre-Jacques Liotier

Composites: Part A 187 (2024) 108496

Contents lists available at ScienceDirect

Composites Part A

journal homepage: www.elsevier.com/locate/compositesa

Influence of the surface energy of a basalt fiber on capillary wicking and in-plane permeability of reinforcements

Romain Ravel [a,*], Monica Francesca Pucci [b], Pierre-Jacques Liotier [a]

[a] Polymers Composites and Hybrids (PCH), IMT Mines Ales, Ales, France
[b] LMGC, Univ Montpellier, IMT Mines Ales, CNRS, Ales, France

ARTICLE INFO

Keywords:
Wettability
In-plane permeability
Capillary wicking
Liquid composite molding

ABSTRACT

This study evaluates the influence of a thermal treatment of a basalt fiber on capillary wicking tests and in-plane permeability experiments, under several pressure differences. The impact of the treatment was characterized at three scales: microscopic, to determine the fiber surface energy; mesoscopic, to estimate an equivalent capillary pressure (P_{cap}) of the fabric in spontaneous impregnation; and macroscopic, to determine the saturated (K_{sat}) and unsaturated (K_{unsat}) permeability of the fibrous preform at the process scale. Results at the microscopic scale showed that the thermal treatment increased the polarity of the fiber by 22% and decreased its surface roughness. Capillary wicking tests showed that the treated fabric presents a better affinity with water, increasing P_{cap} by 68%. At the process scale, permeability experiments showed the increase of K_{sat} and K_{unsat} after treatment. Finally, results of capillary pressure (ΔP_{γ}) showed a dominance of capillary effects under the negative pressure difference.

1. Introduction

Liquid Composites Molding (LCM) processes are used in a wide range of industrial sectors, and particularly in the energy and transport sectors, to manufacture composite materials [1,2]. The aim of these processes is to impregnate a stack of fabrics with a liquid resin. The impregnation can be performed by applying a pressure on the fluid at the inlet (resin transfer molding or RTM) [3] or by applying a partial vacuum at the mold outlet using a vacuum pump (vacuum assisted resin transfer molding or VARTM) [4]. In both cases, the fluid flows through the fibrous preform from the highest pressure to the lowest. One of the crucial challenges of these processes for obtaining a satisfying part quality is the good impregnation of the fibrous preform before resin curing [5]. Defects in impregnation lead to the formation of voids which affects the surface quality and the mechanical properties of the final parts [6,7]. The key for the successful impregnation is the synergy between the process parameters, the fluid properties and the fibrous preform properties.

The fibrous preform is generally characterized by a parameter referred to as permeability. The permeability (K) is an intrinsic parameter of the porous medium and defines its ability to allow a fluid to flow through it. Permeability can be estimated once the mold is fully filled with liquid, referred as saturated permeability (K_{sat}) or when the fluid is filling the mold, that is the unsaturated permeability (K_{unsat}) [8]. According to the Gebart law, the permeability only depends on the geometry and the porosity of the porous medium [9]. However, in the literature, several works showed that the unsaturated permeability, determined with the "squared flow front method", could also depend on the fluid-fiber physico-chemical interactions, including the fiber roughness, during the process [10,11]. The morphology of the porous medium can be modeled as either a single scale porous medium (random fiber mat [12]) or a double pore scale (woven fabric: intra-tows pores, between single fibers and inter-tows pores, between tows [13–15]). The double pore scale can lead to a double flow scale during the impregnation and consequently rise the risk of void entrapment. In literature, many studies relate to the competition between the viscous forces and the capillary effects which tend to the formation of micro-voids inside the tows when viscous forces are greater than capillary effects or macro-voids between the tows when capillary effects are greater than viscous forces [10,13,15,16]. The majority of them already linked the different parameters (liquids properties, preform architecture, process parameters) to the saturated and unsaturated permeability. The four permeability benchmark exercises showed the importance of the human factor, the experimental procedure, the data analysis method and the liquid nature for a defined porous medium [17–20]. These studies led to the edition of a standard in July 2023 to standardize the method of characterizing unsaturated in-plane permeability [21]. Other works showed that the architecture, the shearing of

* Corresponding author.
E-mail address: romain.ravel@mines-ales.fr (R. Ravel).

https://doi.org/10.1016/j.compositesa.2024.108496
Received 1 July 2024; Received in revised form 26 September 2024; Accepted 27 September 2024
Available online 9 October 2024

the fabric or the fiber volume fraction also impact the permeability [22–25]. Some studies focused on the estimation of a capillary pressure at the process scale during the process [10,11,26]. Caglar et al. [11] showed, using capillary wicking tests and permeability experiments (saturated and unsaturated), that by modifying a glass fabric via a corona treatment, the wetting behavior of the treated fabric has been improved. Authors calculated the ratio $R_s = K_{unsat}/K_{sat}$, and found a R_s value higher than 1 after treatment, revealing the presence of capillary effects during the process in the study conditions.

The present study is thus part of the scientific debate about the importance of taking into account the capillary effects during the impregnation and particularly of its effect on the characterization of the unsaturated permeability. This work used innovating tensiometric methods to determine the surface energy of the single basalt fiber [27] and to determine an equivalent capillary pressure from capillary wicking tests [28]. Moreover, it is the first time that saturated and unsaturated permeability experiments were also studied with a pressure difference below the atmospheric pressure, as in the VARTM conditions.

The main originality of the present work is to modify the physico-chemical affinity between the basalt fiber and water by using a thermal treatment and to evaluate at different scales (micro, meso and macro) the impact of the treatment on capillary wicking tests and in-plane permeability experiments, setting different pressure gradients.

The basalt fabric chosen was thermally treated to modify its surface properties [29]. Then at a microscopic scale, the surface and the morphology of the single fiber were characterized by scanning electron microscopy (SEM) and atomic force microscopy (AFM). The surface energy of the single basalt fiber (with polar and dispersive components) has been determined before and after treatment with a force tensiometer. At a mesoscopic scale, capillary wicking tests were performed to evaluate the influence of the surface modification on the fabric behavior in spontaneous impregnation with water. An apparent advancing contact angle and an equivalent capillary pressure have been determined with a tensiometric method developed by Pucci et al. [28]. Finally, following the standard [21], saturated, and unsaturated permeability experiments with water were performed in different cases of pressure difference (RTM case: 60 kPa, 100 kPa and VARTM case: 60 kPa, 80 kPa below the atmospheric pressure) to evaluate the influence of the surface modification of the fabric at the process scale. The ratio R_s (K_{unsat}/K_{sat}) and the capillary pressure at the process scale (ΔP_γ) as used by Caglar et al. [11] were estimated to evaluate the balance between capillary effects and viscous forces before and after treatment in the studied conditions.

2. Materials and methods

2.1. Materials

2.1.1. Basalt fibers

Untreated basalt fiber

The quasi-unidirectional basalt fabric chosen for this study was supplied by BASALTEX NV (Belgium, Wevelgem, reference BAS UD400). The fiber material has a density of 2.67 g/cm^3. This fabric has an areal weight of 430 g/m^2 and its weft direction is composed of heat-bonded glass yarns. The fibers present a silane-based sizing compatible with epoxy resins. In this work, the untreated fibers and fabrics are called "as received" or "AR".

Treated basalt fiber

To modify the surface energy of the basalt fiber, a thermal treatment of 4 h at 400 °C (under air) in a LENTON Furnaces oven (Fairland, Randburg, South Africa) was carried out, according to a previous work [29]. Pucci et al. showed that this treatment leads to a significant increase of the surface energy of the basalt fiber surface and particularly of its polar component. The treatment was performed on the tows for the surface energy determination, on the rolls of fabric for the capillary wicking tests and on plies of fabric for the permeability experiments. The modified fibers and fabrics after thermal treatment are called "thermally treated" or "TT" in the study.

Table 1
Test liquid properties at 20 °C [29].

Test liquids	η [mPa s]	ρ [g/cm^3]	γ_L^p [mN/m]	γ_L^d [mN/m]	γ_L [mN/m]
N-hexane	0.32	0.659	0.0	18.4	18.4
Diiodomethane	2.76	3.325	2.3	48.5	50.8
Ethylene glycol	21.81	1.113	19	29	48
Water	1.00	0.998	51.0	21.8	72.8

2.1.2. Test liquids

N-hexane (n-hex), diiomomethane (diiodo), ethylene glycol (EG) and water were used to determine the surface energy of the single basalt fiber before and after thermal treatment. Table 1 presents for each liquid: the viscosity (η), the density (ρ), the polar (γ_L^p) and dispersive components (γ_L^d) and the total surface tension (γ_L). N-hexane and water were used for capillary wicking tests, whereas only water was used for the permeability measurements in first approach.

2.2. Methods

2.2.1. Morphological characterizations of fibers by scanning electron microscopy (SEM) and atomic force microscopy (AFM) analyses

The surface morphology of basalt fibers was observed before and after thermal treatment by SEM and AFM to analyze the homogeneity and the distribution of the sizing on the single fiber. The aim was to characterize the fiber morphology after a partial or complete un-sizing of the basalt fiber due to the thermal treatment.

Scanning electron microscopy

The SEM analyses were performed in a QUANTA 200 FEG microscope supplied by FEI (Hillsboro, USA), operating at 10 kV. In order to minimize the material degradation during the analyses, fibers were previously metallized with a carbon braid metallizer CED 030, supplied by Balzers, during 15 min at 10^{-2} mbar.

Atomic force microscopy

The atomic force microscope used was a MFP-3D Infinity supplied by Asylum Research (Santa Barbara, USA), operating in a tapping mode in order to obtain images of fiber surface topography. Three areas of 3 × 3 μm^2 per fiber and two fibers per reference (AR and TT) were analyzed to assess the reproducibility. Data obtained by AFM were post-processed with the open source software "Gwiddion" to obtain three-dimensional topography images of the fiber surfaces [30]. Aiming at characterizing the roughness of the fibers, two parameters were evaluated: the root mean square value S_q (Eq. (1)) and the maximum height in absolute value S_p [30–32].

$$S_q = \sqrt{\frac{1}{A}\iint_A z^2(x,y)\,dx\,dy} \tag{1}$$

where A is the analyzed area and z, the surface height defined for each acquired data at a position x (abscissa) and y (ordinate).

Diameter characterization

The average diameter of the single fiber before and after thermal treatment was characterized both by SEM analysis and by the tensiometric method, as detailed in Section 2.2.2.

2.2.2. Tensiometric characterization

To determine the surface energy of the single basalt fiber, contact angles between a single fiber and several test liquids were characterized with a K100SF force tensiometer supplied by KRŮSS (Germany). This equipment measures the mass of the meniscus formed by the liquid around the single fiber, by using a high precision balance with a 10^{-7} g resolution. This tensiometric method was clearly described by W. Garat et al. [27]. By using the Wilhelmy equation (Eq. (2)), it is possible to determine a static contact angle θ_e for each liquid-fiber couple:

$$F_c = ma = p\gamma_L \cos\theta_e \tag{2}$$

where F_c is the capillarity force, m is the meniscus mass, a the acceleration, p the wetting perimeter and γ_L is the liquid surface tension.

The method is constituted by different steps. In the first one, the single fiber is bonded onto a support with a UV adhesive (Dymax Europe GmbH, reference: 3193). Secondly, an experiment with a totally wetting liquid, the n-hexane ($\theta_e \simeq 0°$), is performed to determine the wetting perimeter. This perimeter value is also used to calculate the average diameter of the single fiber. Finally, by making tests on the same fiber, the static contact angles (θ_e) are determined with three other liquids: diiodomethane, ethylene glycol and water (Table 1) [27]. Five experiments for each reference (AR and TT) and each liquid were performed to assess the reproducibility.

2.2.3. Surface energy determination

Through the combination of the Owens and Wendt equation (Eq. (3)) and the Young–Laplace equation (Eq. (4)), one obtains Eq. (5), which enables the determination of the surface energy of the fibers (γ_S).

$$\gamma_S + \gamma_L - \gamma_{SL} = 2\sqrt{\gamma_S^d \gamma_L^d} + 2\sqrt{\gamma_S^p \gamma_L^p} \tag{3}$$

$$\cos\theta_e = \frac{\gamma_S - \gamma_{SL}}{\gamma_L} \tag{4}$$

$$\gamma_L(1+\cos\theta_e) = 2\sqrt{\gamma_S^d \gamma_L^d} + 2\sqrt{\gamma_S^p \gamma_L^p} \tag{5}$$

More precisely, using the static contact angle values (θ_e) determined previously for the different test liquids, the polar (γ_S^p) and dispersive (γ_S^d) components of the surface energy can be calculated through Eq. (5). Then, by dividing Eq. (5) by $2\sqrt{\gamma_L^d}$, a linearized form of the Owens and Wendt equation is obtained, as follows:

$$\underbrace{\frac{\gamma_L(1+\cos\theta_e)}{2\sqrt{\gamma_L^d}}}_{Y} = \underbrace{\sqrt{\gamma_S^p}\left(\frac{\sqrt{\gamma_L^p}}{\sqrt{\gamma_L^d}}\right)}_{X} + \sqrt{\gamma_S^d} \tag{6}$$

The parameters Y and X of Eq. (6) are calculated for each liquid with the contact angle (θ_e) determined experimentally and the liquid properties presented in Table 1. Then, by drawing the curve Y as a function of X, the polar (γ_S^p) and dispersive (γ_S^d) components of the fiber surface energy can be calculated through the linear regression (Eq. (6)).

2.2.4. Capillary pressure determination: wicking tests

Capillary wicking tests have been performed with a DCAT11 force tensiometer supplied by Dataphysics Instrument GmbH (Germany) with a 10^{-5} g resolution, according to a methodology described in a previous work [28]. The experiment consists in inserting a roll of fabric in a cylindrical sample holder with 12 mm diameter and 20 mm height. Capillary wicking is here studied in the direction parallel to the fiber orientation. According to the fabric properties, a fabric strip, measuring 236 mm length by 20 mm height, has to be cut to obtain a fiber volume fraction of 40% in the sample holder. The fabric strip is rolled up and inserted into the sample holder. Then the sample holder is suspended on the balance and a vessel containing the liquid is placed under it. The vessel moves up at a speed of 0.5 mm/s until it touches the fabric. After contact, the vessel stops and the mass corresponding to the liquid wicking in the fabric is recorded over the time. First, through the modified Washburn equation for a porous medium in a tube (Eq. (7)), the morphological parameter of the porous medium ($c\bar{r}$) can be determined experimentally with a totally wetting liquid, the n-hexane:

$$m^2(t) = \left[\frac{(c\bar{r})\varepsilon^2(\pi R^2)^2}{2}\right]\frac{\rho^2\gamma_L\cos\theta_a}{\eta}t \tag{7}$$

where c is a parameter relative to the tortuosity of the medium, $\bar{r}$ is a parameter representative of the mean capillary radius, ε is the relative porosity, R is the inner radius of the sample holder, ρ is the density, η is the viscosity, θ_a is the apparent advancing contact angle and γ_L is the total surface tension of the liquid. As θ_a is considered as null using the totally wetting liquid, Eq. (7) can be simplified as follows:

$$m^2(t) = \frac{(c\bar{r})\varepsilon^2(\pi R^2)^2\rho^2\gamma_L}{2\eta}t \tag{8}$$

The slope of the linear part of the squared mass against time (Fig. 1(a)), using n-hexane, allows the determination of the morphological parameter of the porous medium ($c\bar{r}$). Then, by knowing the value of $c\bar{r}$, a second experiment with water is performed to determine the apparent advancing contact angle θ_a, calculated from Eq. (7) with the fit of the squared mass over time, as shown in Fig. 1(b).

Finally, an equivalent capillary pressure can be estimated according to the method used by Pucci et al. [28]. The definition of the equivalent capillary pressure (P_{cap}) in this work is based on an equivalence between the Darcy law and the Washburn equation for the capillary wicking in a porous medium, as follows:

$$P_{cap} = (c\bar{r})\varepsilon\frac{\gamma_L\cos\theta_a}{4K} \tag{9}$$

where ($c\bar{r}$) represents the morphology of the porous medium as defined above, ε is the porosity of the porous medium, K is the theoretical saturated permeability of the porous medium according to Gebart theory [9] with an hexagonal arrangement, γ_L is the surface tension of the liquid and θ_a is the apparent advancing contact angle representing the fluid/porous medium interactions. In the present case, the hexagonal arrangement is an assumption due to a lack of data to choose the most representative arrangement for our sample in the cylindrical sample holder. Five experiments of capillary wicking with water for each reference (AR and TT) were performed to assess reproducibility.

2.2.5. In-plane permeability measurements

Saturated (K_{sat}) and unsaturated (K_{unsat}) permeability measurements were performed to characterize the effect of the fiber surface modification at the process scale. These experiments were performed by means of a permeability setup developed and made in IMT Mines Alès (Fig. 2(a)). This permeability characterization setup complies with the standard ISO 4410:2023 [21]. The setup is composed of a top mold in transparent poly(methyl methacrylate) (PMMA) with 100 mm thickness, a bottom mold in aluminium (20 mm thickness) and an aluminium frame (2.94 mm thickness). The frame is placed between the two parts of the mold to receive the fibrous preform. The internal dimensions of frame cavity are 400 mm × 150 mm × 2.94 mm as shown in Fig. 2(b).

The inlet is placed on the left side of the fibrous preform and the outlet, on the right side, allowing to perform a permeability test with a rectilinear flow (1-D) (Fig. 2(b)). Silicone grease is applied around the preform cavity and between the mold parts (bottom/frame/top) to ensure the sealing. The mold is locked with sixteen screws tightened with a torque of 25 N m. The bottom mold is instrumented with two pressure sensors localized as close as possible to the inlet and outlet holes (Keller, PR35X series). In first approach, the chosen test liquid was water. According to Pucci et al. [29], water is a good candidate to exhibit significant effects due to its chemical affinity with the high polar surface of the unsized basalt fiber, in addition to its ease of cleaning. For each test, ten plies of basalt fabric were placed in the frame of 2.94 mm thickness, which represents a fiber volume fraction of 54.8%.

Unsaturated permeability determination

According to the literature [19], the in-plane unsaturated permeability is determined by the squared flow front position method. The flow front acquisition is recorded with a color camera (reference EXO252CU3) supplied by SVS-Visteck, and equipped with a fixed lens 12 mm/F2.8 (reference M1228-MPW3), supplied by Computar. During the experiments, the advancing fluid front position is recorded as a function of time with a frequency of 5 Hz. The pressure values at the inlet and outlet are recorded with the same frequency to determine the pressure difference along the preform. Finally, images are processed with a LabVIEW program developed at IMT Mines Alès. Firstly, the

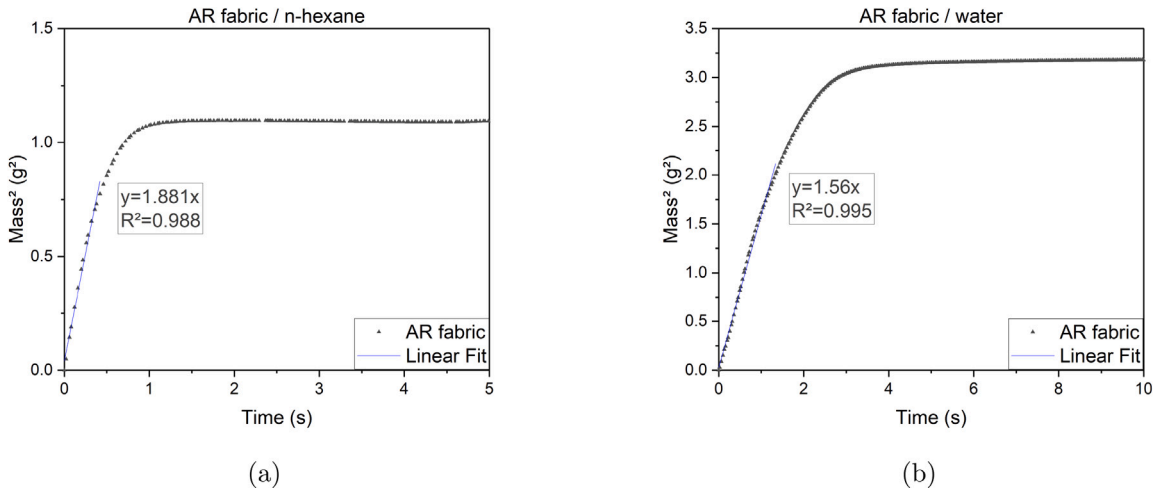

Fig. 1. Capillary wicking tests with n-hexane (a) and water (b) - AR fabric.

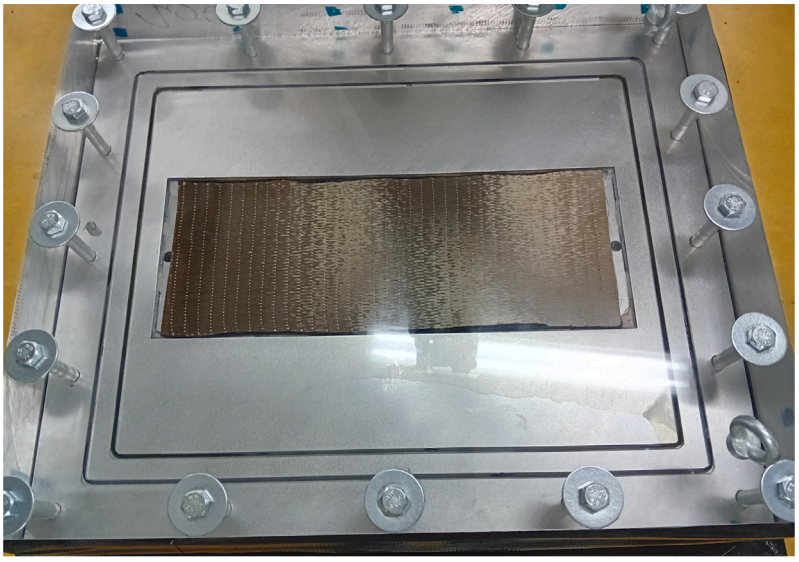

Fig. 2. Permeability setup (a) and internal dimensions of the cavity (b).

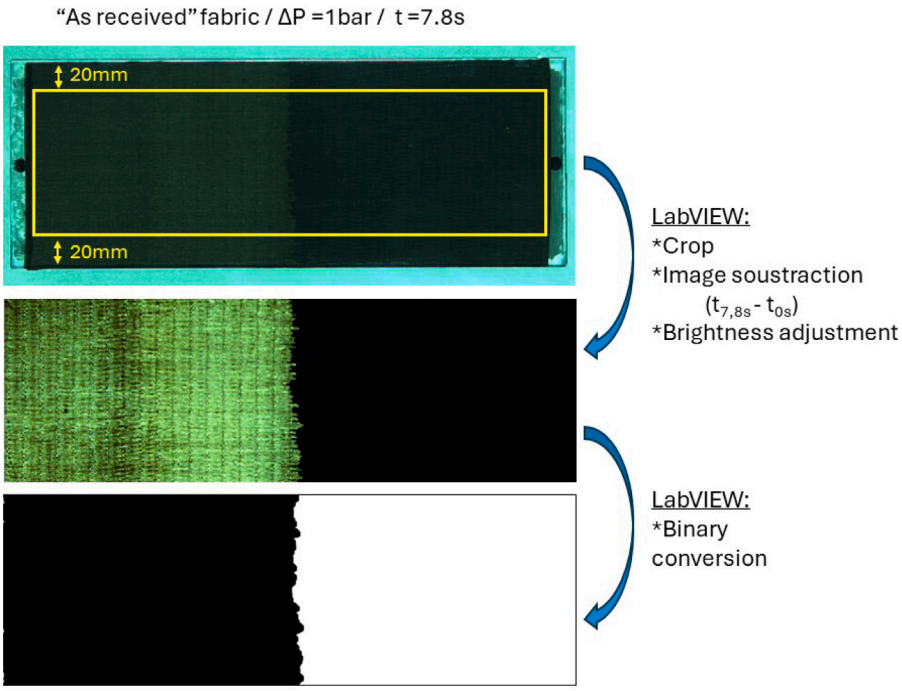

Fig. 3. Unsaturated permeability determination : image processing with LabVIEW.

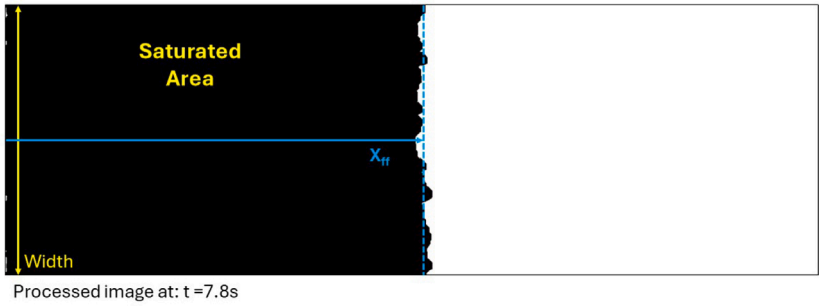

Fig. 4. Unsaturated permeability determination : x_{ff} calculation method.

images are cropped to avoid the edge effect (20 mm), then by adjusting the color contrast, the saturated area is converted into a black area (Fig. 3). The value of the average fluid front position x_{ff} is calculated by dividing the surface area saturated with fluid by the width of the crop (Fig. 4). After processing all images, the curve of the squared flow front position x_{ff}^2 as a function of time is drawn as shown in Fig. 5.

The squared flow front method used to determine the unsaturated permeability was clearly described in the second permeability benchmark of Vernet et al. [19]. The curve x_{ff}^2 against time can be plotted as a linear fit. Then, according to the Darcy law, the slope β of the linear fit allows to calculate the unsaturated permeability (Eq. (10)):

$$K_{unsat} = \frac{x_{ff}^2}{t}\frac{\varepsilon\eta}{2\Delta P} = \beta\frac{\varepsilon\eta}{2\Delta P} \tag{10}$$

where β is the slope of the linear fit of the curve x_{ff}^2 against time, ε is the relative porosity, η is the fluid viscosity and ΔP is the pressure difference along the fiber preform.

Saturated permeability determination

The saturated permeability is determined using a balance placed at the outlet of the permeability setup. After the total saturation of the fibrous preform, the fluid flows in a tank placed on the balance. The weight of the fluid as a function of time is recorded with a frequency of 1 Hz. Then the fluid mass is converted in volume using the fluid density. The volumetric flow rate Q (m^3/s) can be determined through

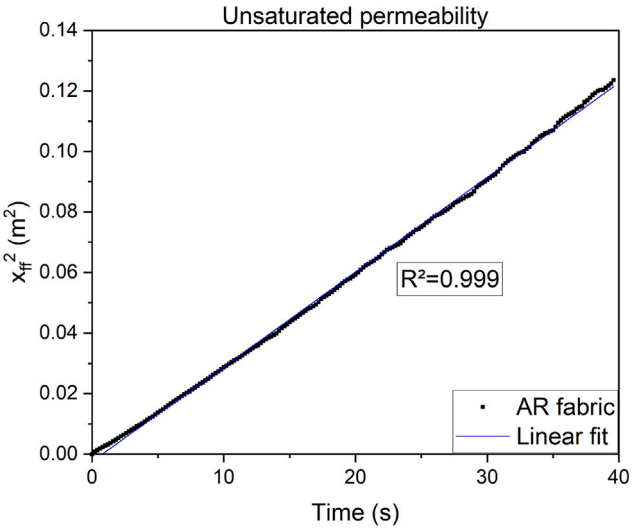

Fig. 5. Unsaturated permeability determination : squared flow front position vs. time.

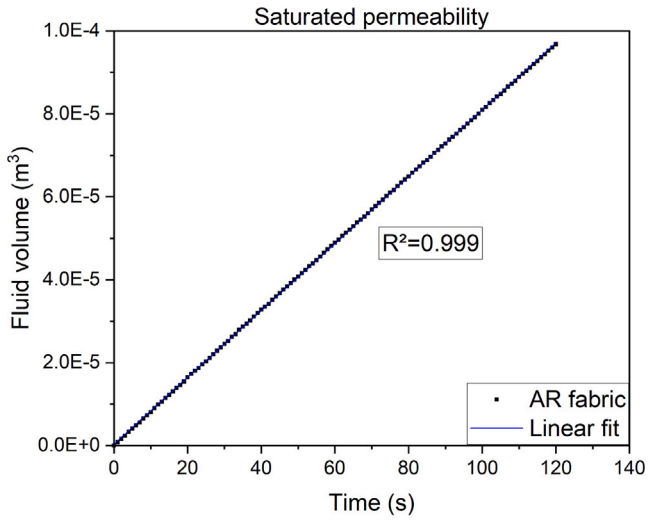

Fig. 6. Saturated permeability determination : fluid volume against time.

Table 2
Experimental conditions for permeability experiments.

As received fabric		Thermally treated fabric	
$K_{unsaturated}$	$K_{saturated}$	$K_{unsaturated}$	$K_{saturated}$
60, 100 kPa −60, −80 kPa	60, 100 kPa −60, −80 kPa	60, 100 kPa −60, −80 kPa	60, 100 kPa −60, −80 kPa

the slope of the linear fit of the curve of fluid volume as a function of time (Fig. 6). Finally, by using the Darcy law (Eq. (11)) [33] saturated permeability can be calculated as following:

$$K_{sat} = \frac{Q\eta\Delta L}{A\Delta P} \tag{11}$$

where Q is the volumetric flow rate determined experimentally, ΔL is the preform length, A is the transverse area of the mold cavity and ΔP is the pressure difference along the fiber preform.

Pressure conditions

In the study, the pressure conditions are expressed as relative pressures, meaning that the pressure difference above the atmospheric pressure has been referred as a positive value, and the pressure difference below the atmospheric pressure (partial vacuum condition) has been referred as a negative value. Of course, a positive value is used in both cases to estimate permeability values from the Darcy law. To evaluate the influence of the pressure difference in different process configurations, two relative pressure conditions were applied:

- a positive relative pressure, applied at the inlet, referred as “RTM case” in the study, with a single component injection tank, supplied by ISOJET Equipements (Corbas, France), at 60 kPa and 100 kPa.
- a negative relative pressure, applied at the outlet, referred as “VARTM case” in the study, with a Compositvac mobile E25, supplied by Diatex (Saint Genis Laval, France), at −60 kPa and −80 kPa.

Low pressure conditions were chosen compared to the pressure commonly used in the RTM process. The aim was to obtain a configuration where the capillary pressure, due to capillary effects, can be comparable to the imposed pressure. Furthermore, to compare the two pressure conditions (pressure and partial vacuum), the maximum value was limited to a null absolute pressure (≃−100 kPa in relative pressure). Three experiments were performed for each condition (Table 2) to assess the reproducibility.

Finally, according to the literature [11,13,34,35], the ratio R_s and its associated capillary pressure ΔP_γ were estimated to identify the influence of the capillary effects at the process scale with the following relation:

$$R_s = \frac{K_{unsat}}{K_{sat}} = 1 - \frac{\Delta P_\gamma}{\Delta P} \tag{12}$$

where K_{unsat} is the unsaturated permeability, K_{sat} is the saturated permeability, ΔP_γ is the estimated capillary pressure at the process scale and ΔP is the pressure difference applied. According to the literature, this relation is valid only when the sink effect is negligible [36,37]. This effect has been highlighted for a flow rate controlled impregnation and a double pore scale. For applied pressure difference without flow rate monitoring, it was assumed that the sink effect can be neglected. This assumption can be considered as acceptable since, in this study, permeability is estimated at the scale of the homogeneous equivalent medium and the yarn scale is not considered [38].

Table 3
Basalt fibers diameters before and after thermal treatment, measured by SEM and tensiometric method.

Method	Average diameter ($\bar{d} \pm SD$) [μm]	
	AR fibers	TT fibers
SEM images	18.3 ± 0.5	18.9 ± 0.6
Tensiometry	18.3 ± 0.8	18.5 ± 1.9

3. Results and discussion

3.1. Morphological characterizations

To characterize the diameter and the surface morphology of the basalt fibers before and after thermal treatment, fibers were analyzed by SEM, AFM and the tensiometric method. First, fiber diameters were determined before and after thermal treatment using SEM and the tensiometric method. Table 3 presents the diameters measured with both methods. Results are very similar, with a low standard deviation, leading to the conclusion that the thermal treatment did not affect the fiber diameter. Moreover, these results confirm the reliability of the diameter measurement by the tensiometric method using the K100SF.

The sizing distribution and homogeneity were characterized by SEM and AFM. Figs. 7 and 8 present SEM images before and after thermal treatment, respectively. For the AR fiber, Fig. 7(a) shows the presence of large deposits of sizing (between 3 and 5 μm) bonded to the fibers. Fig. 7(b) also shows the presence of small deposits distributed all along the fiber. After thermal treatment, Fig. 8 shows that the deposits are still present but with a smaller size. In order to thoroughly investigate these observations, AFM analyses were performed to characterize topography and to quantify the fiber roughness.

Fig. 9 shows images of fiber topography obtained by AFM for the AR and TT fiber. Data associated to images were processed with the open source software “Gwiddion” to reconstruct the fiber curvature and calculate surface roughness. Table 4 presents the roughness results characterized by the parameters S_q (the root mean square) and S_p (the maximum height in absolute value), as defined in Section 2.2.1 (i.e. correcting the effect of the curvature). As shown in Table 4, the surface roughness of the AR basalt fiber is different for the two fibers analyzed, with S_q and S_p values significantly far from each other. On the contrary, for the TT basalt fibers, S_p values are lower than for the AR fibers, and S_q values are more significantly similar. It appears that the AR fiber has a non-uniform sizing distribution, with small and big deposits distributed over the entire surface of fibers. After thermal treatment, the biggest deposits of sizing were no more observed, only smaller deposits remained. The surface of the TT basalt fiber tends to be smoother and more homogeneous compared to the AR fiber.

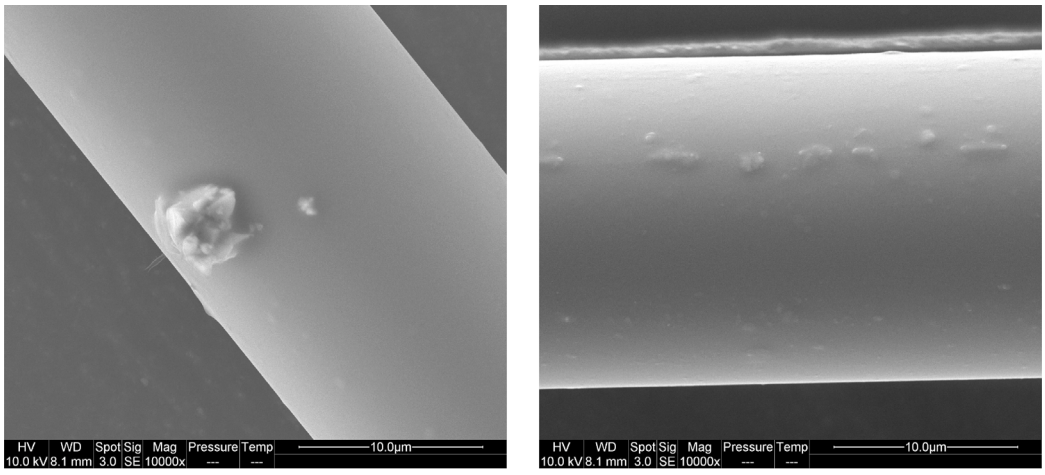

Fig. 7. SEM observations of the AR basalt fiber.

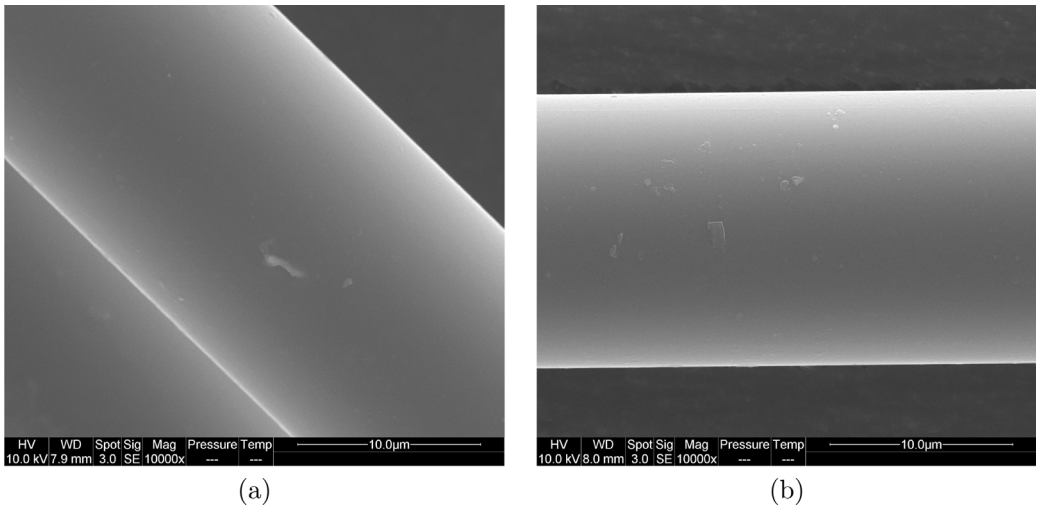

Fig. 8. SEM observations of the TT basalt fiber.

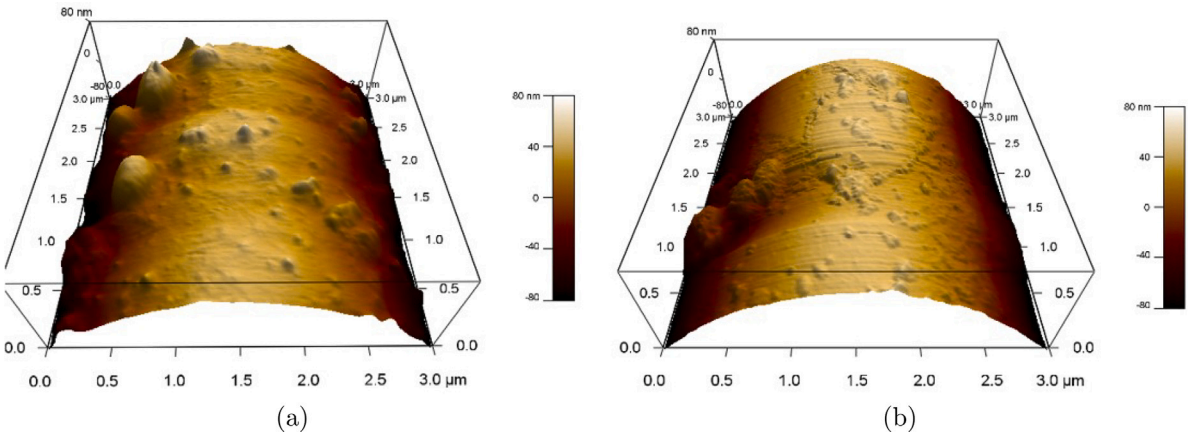

Fig. 9. AFM observations of the AR (a) and TT (b) basalt fiber.

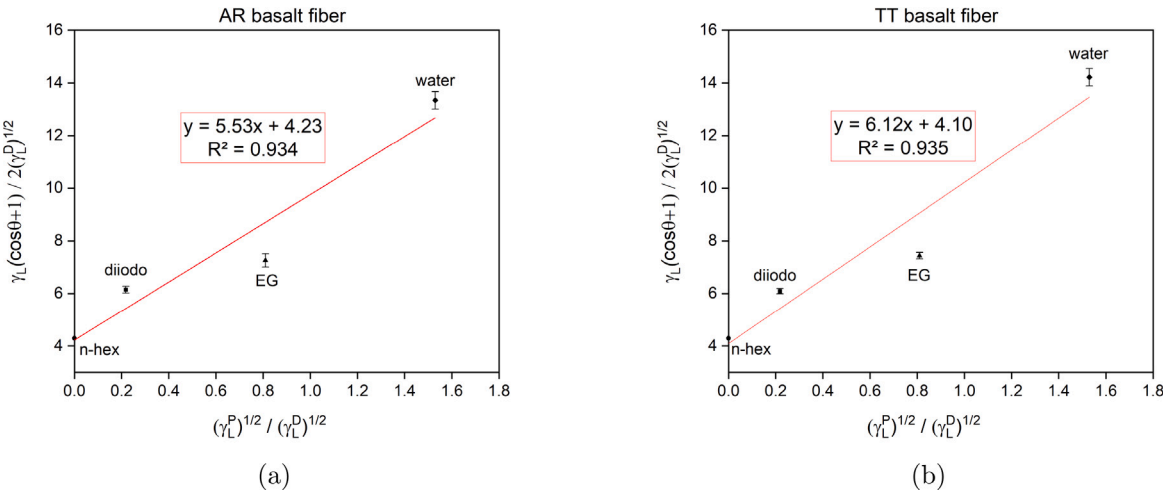

Fig. 10. Application of the Owens and Wendt method for surface energy determination of AR (a) and TT (b) basalt fiber.

Table 4
AFM results (S_p and S_q) before and after thermal treatment.

	AR fabric		TT fabric	
	Fiber 1	Fiber 2	Fiber 1	Fiber 2
S_p [nm]	82.4 ± 28.5	113.1 ± 10.5	67.3 ± 12.3	63.3 ± 7.8
S_q [nm]	4.5 ± 1.2	13.2 ± 4.2	5.5 ± 1.6	5.6 ± 0.8

Table 5
Static contact angles of basalt fibers before and after thermal treatment.

Average values	θ_e n-hex [°]	θ_e water [°]	θ_e diiodo [°]	θ_e EG [°]
AR basalt fiber	0	44.6 ± 3.4	51.0 ± 4.0	46.7 ± 2.7
TT basalt fiber	0	34.5 ± 4.1	48.0 ± 2.0	47.9 ± 2.0

3.2. Contact angle determination for single fiber

Table 5 presents results of the average static contact angles before and after thermal treatment with the four test liquids (n-hexane, diiodomethane, ethylene glycol and water). For diiodomethane and ethylene glycol, the static contact angles are similar before and after treatment. However, with water, the static contact angle after thermal treatment decreases by 23% (from 44.6° to 34.5°). This decrease shows that the water presents greater affinity and better wettability with the TT basalt fiber.

3.3. Fiber surface energy determination

The application of Owens and Wendt method for both references (AR and TT) enables the determination of the surface energy of the single basalt fiber, taking into account the static contact angles obtained previously, as shown in Fig. 10. It can be observed that, in both cases, the results are in accordance with the Owens and Wendt equation with a minimum correlation coefficient of 0.93. Table 6 presents the calculated values of surface energy. After thermal treatment, the total surface energy γ_s increases from 48.5 mN/m to 54.3 mN/m. This increase is mainly due to the rise of the polar component (+22%). This result is in accordance with other works from literature having already shown that the unsized basalt fiber presents a stronger polarity than the sized one [29,39].

3.4. Capillary wickings tests

3.4.1. Determination of the morphological parameter

As described in Section 2.2.4, the morphological parameter $c\bar{r}$ is determined experimentally with the n-hexane according to the Washburn equation (Eq. (7)). Fig. 11(a) and (b) show the curves of the squared mass as a function of time respectively for the AR and TT fiber using n-hexane. Curve slopes have been calculated at the first 0.4 and 0.7 s for the AR and the TT fabric respectively. For both reinforcements, the first part of the curves before the mass stabilization, can be fitted with a linear trend. Table 7 presents the slope w^2/t values, the correlation coefficient of the slope R^2 and the $c\bar{r}$ values for the AR and TT fabrics. All correlation coefficients are higher than 0.97, confirming a good correspondence with the Washburn equation. The slope is significantly higher for the AR fabric, which means that the rise of n-hexane is faster, leading to greater values for the $c\bar{r}$ factor. This unexpected difference of $c\bar{r}$ after treatment could be related to a morphological modification caused by the thermal treatment and more specifically to a difference of roughness according to AFM results.

Table 6
Dispersive (γ_s^d), polar (γ_s^p) and total (γ_s) surface energy of the AR and TT basalt fibers.

Basalt fiber	γ_s^p [mN/m]	γ_s^d [mN/m]	γ_s [mN/m]
AR	30.6 ± 2.1	17.9 ± 0.4	48.5 ± 2.5
TT	37.5 ± 2.3	16.8 ± 0.1	54.3 ± 2.4

Table 7
w^2/t, R^2 and $c\bar{r}$ results from the capillary wicking tests with n-hexane for AR and TT fabrics.

AR fabric	w^2/t [g²/s]	R^2	$c\bar{r}$ [µm]
Test 1	1.881	0.988	32.7
Test 2	1.802	0.980	31.3
Test 3	1.990	0.980	34.6
Test 4	1.620	0.971	28.2
Test 5	1.477	0.977	25.7
$MEAN \pm SD$	1.754 ± 0.206		30.5 ± 3.6
TT fabric	w^2/t [g²/s]	R^2	$c\bar{r}$ [µm]
Test 1	0.955	0.982	16.6
Test 2	0.942	0.999	16.4
Test 3	1.072	0.988	18.6
Test 4	1.085	0.978	18.9
Test 5	0.908	0.975	15.8
$MEAN \pm SD$	0.992 ± 0.080		17.3 ± 1.4

3.4.2. Determination of the apparent advancing contact angle

Fig. 12(a) and (b) present the curves of the squared mass as a function of time respectively for the AR and TT fibers with water. The first part of the curves can be fitted with a linear trend. The slopes of the curves (w^2/t) were calculated at the first 1.3 and 0.7 s

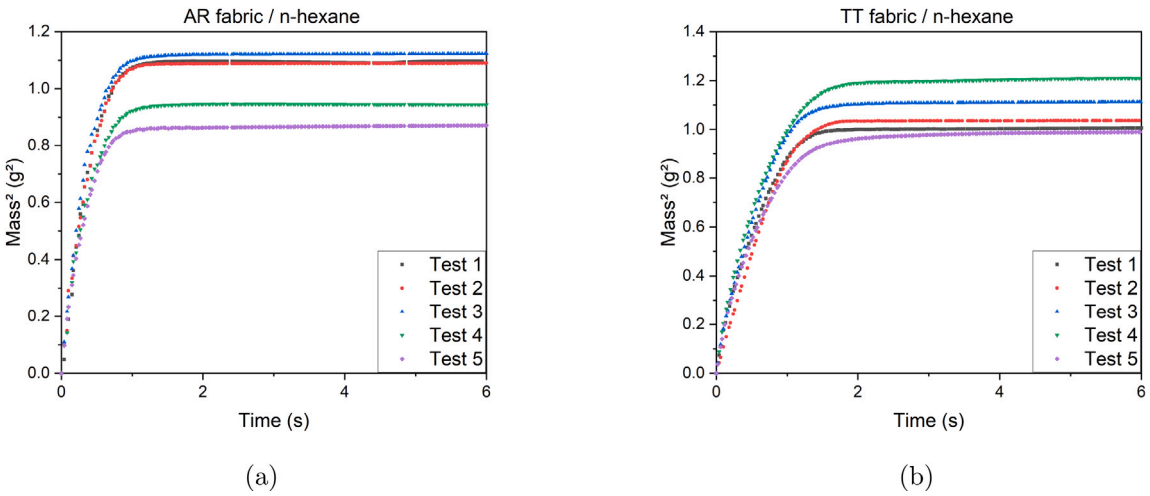

Fig. 11. Capillary wicking tests: AR (a) and TT (b) fabrics with n-hexane.

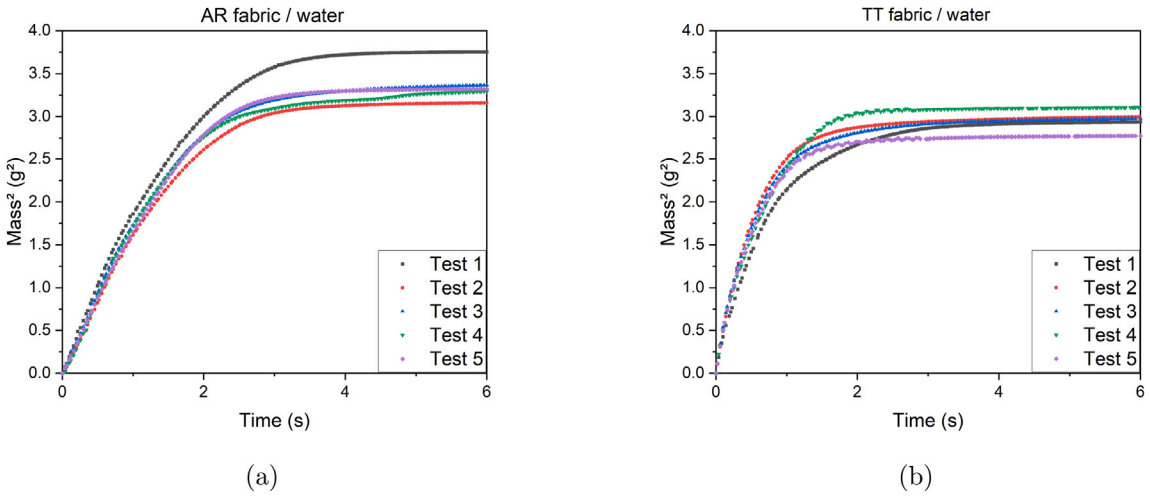

Fig. 12. Capillary wicking tests: AR (a) and TT (b) fabrics with water.

respectively for the AR and the TT fabrics. Table 8 presents the results of the slope w^2/t, the correlation coefficient of the slope (R^2) and the apparent advancing contact angle θ_a with water for both fabrics. θ_a was calculated from Eq. (7) with the average $c\bar{r}$ factor obtained experimentally previously (Table 7). The correlation coefficients of the slopes are higher than 0.97, which confirm a good correspondence with the Washburn equation. Capillary wicking is faster in the thermally treated fabric, with an average slope of 2.7 g^2/s compared to 1.6 g^2/s for the AR fabric. Results of mean apparent advancing contact angles θ_a are presented in Table 8. The mean apparent advancing contact angle θ_a decreases from 71.2° ± 0.9° for the AR fabric to 17.2° ± 12.3° for TT fabric. This large decrease is due to the faster capillary rise and to the decrease of the $c\bar{r}$ factor. This faster capillary rise is a consequence of the wettability improvement between the water and the TT basalt fiber, as shown at the microscopic scale. The θ_a is a dynamic parameter and it cannot be compared with the static contact angle obtained previously (Table 5), but a contact angle decrease after thermal treatment is observed at both scales. More importantly, as described by Pucci et al. [28], physically, this θ_a cannot be defined as an advancing contact angle as it is for the capillary ascension in a tube. Actually, it is a characteristic value associated to the fluid-fiber interaction for a fiber volume fraction and a defined porous medium morphology.

Table 8
w^2/t, R^2 and $\theta_a water$ results from the capillary wicking tests with water for AR and TT fabrics.

AR fabric	w^2/t [g^2/s]	R^2	$\theta_a$water [°]
Test 1	1.744	0.990	70.0
Test 2	1.560	0.995	72.2
Test 3	1.637	0.992	71.2
Test 4	1.694	0.992	70.6
Test 5	1.589	0.996	71.8
$MEAN \pm SD$	1.645 ± 0.076		71.2 ± 0.9
TT fabric	w^2/t [g^2/s]	R^2	$\theta_a$water [°]
Test 1	2.423	0.987	32.8
Test 2	2.993	0.976	0.0
Test 3	2.809	0.969	12.9
Test 4	2.626	0.975	24.3
Test 5	2.738	0.972	18.2
$MEAN \pm SD$	2.718 ± 0.212		17.6 ± 12.3

3.4.3. Capillary pressure determination

After determining the morphological parameter $c\bar{r}$ and the apparent advancing contact angle θ_a, the equivalent capillary pressure can be estimated from Eq. (9). Moreover, Ahn et al. [40] proposed a method to determine the capillary pressure in an unidirectional fibrous preform

Table 9
P_{cap} results in spontaneous impregnation with water: comparison between the Pucci et al. and Ahn et al. methods using different contact angles.

Fabric reference	P_{cap} [kPa] Pucci et al. [28] θ_a Washburn	P_{cap} [kPa] Ahn et al. [40] θ_a Washburn	P_{cap} [kPa] Ahn et al. [40] θ_e static
AR	6.5 ± 0.3	3.4 ± 0.2	7.5 ± 0.4
TT	10.9 ± 1.0	9.7 ± 0.6	8.5 ± 0.4

with an one-dimensional flow direction, in spontaneous impregnation, according to Eq. (13):

$$P_{cap} = \frac{F}{D_f}\frac{(1-\epsilon)}{\epsilon}\sigma_L \cos\theta \tag{13}$$

where D_f is the single fiber diameter, ϵ the relative porosity of the fibrous preform, F is a dimensionless form factor ($F = 4$ for a longitudinal flow) and θ, a contact angle representative of the wettability between the unidirectional fibrous preform and the fluid. In a first approach, the static contact angle (θ_e) obtained previously (Table 5), which is a local contact angle, could be used. However, in order to be more representative of the wettability between the unidirectional fibrous preform and the fluid during the capillary wicking experiment, a dynamic contact angle was chosen. The advancing contact angle measured by tensiometric method as described by Garat et al. [27] could be used, but its value depends on the immersion speed of the single fiber in the liquid. Consequently, the apparent advancing contact angle (θ_a) obtained previously with the Washburn method (Table 8) (which represents an apparent contact angle at the level of the equivalent homogeneous porous medium, not dependent on speed), seems to be the most relevant to be use in Eq. (13). Table 9 presents results of capillary pressure in spontaneous impregnation with the different methods, and contact angles for the AR and TT fabrics with water:

- The definition of the equivalent capillary pressure of Pucci et al. [28] with the apparent advancing contact angle θ_a obtained with the Washburn method (Table 8).
- The definition of the capillary pressure of Ahn et al. [40] with the apparent advancing contact angle θ_a obtained with the Washburn method (Table 8).
- The definition of the capillary pressure of Ahn et al. [40] with the static contact angle θ_e obtained with the tensiometric method (Table 5).

After thermal treatment, the equivalent capillary pressure, calculated through the experimental method of Pucci et al. increased from 6.5 kPa to 10.9 kPa. These results show that the thermal treatment of the basalt fiber had an impact on the fiber surface energy, as well as an effect on the fabric behavior in spontaneous impregnation with water, by increasing the equivalent capillary pressure by 68%. In comparison, the capillary pressures calculated with the Ahn et al. definition, using the θ_a or the θ_e, are in the same order and highlight the same tendency to rise after thermal treatment. Furthermore, results obtained with the θ_e are very close to those obtained with the θ_a. In further works, it would be interesting to also estimate the capillary pressure with a third expression often used in the literature (Eq. (14)) [10,41,42] where the form factor S_f represents the surface area of the fluid/fiber interface per unit volume of fluid. This form factor characteristic of the porous media can be experimentally determined with BET analysis (Brunauer–Emmet–Teller specific surface area) [34,43].

$$P_{cap} = -S_f \sigma_L \cos\theta \tag{14}$$

3.5. Permeability measurements

Fig. 13 presents the curves obtained during unsaturated and saturated permeability experiments as in the RTM case (60 kPa and 100 kPa) for the AR and TT basalt fabrics. Tables 10 and 11 present in details all the slope values of the curves $x_{ff}^2 = f(t)$ and $V = f(t)$ and the associated correlation coefficients. The correlation coefficients are all greater than 0.993, showing good accordance with the Eqs. (10) and (11), associated to the determination of the unsaturated and saturated permeability respectively. In each case, the scatter on the slope values on three tests does not exceed 7%, which is small compared to literature [19,20].

Fig. 14 and Tables 12 and 13 present the results obtained from unsaturated and saturated permeability experiments as in the VARTM case (−60 kPa and −80 kPa) for the AR and TT basalt fabrics. The correlation coefficients in each case are greater than 0.997. This means that the linear fits are in accordance with Eqs. (10) and (11). The maximum scatter on the different slope values on three tests does not exceed 10%.

Fig. 15 presents the unsaturated (K_{unsat}) and saturated (K_{sat}) permeability results at 60 kPa and 100 kPa for the AR and TT basalt fabrics. For AR fabric, at 60 and 100 kPa, K_{sat} and K_{unsat} are in the same order. For the TT fabric, the same observation is valid. It means

Table 10
x_{ff}^2/t, V/t and R^2 results from the permeability characterization of the AR and TT fabrics with $\Delta P = 60$ kPa.

$\Delta P = 60$ kPa	$K_{unsaturated}$		$K_{saturated}$	
AR	$x_{ff}^2/t \times 10^{-3}$ [m²/s]	R^2	$V/t \times 10^{-7}$ [m³/s]	R^2
Test 1	3.306	0.999	7.978	0.999
Test 2	3.597	0.999	9.090	0.999
Test 3	3.130	0.999	8,068	0.999
$MEAN \pm SD$	3.344 ± 0.236		8.379 ± 0.617	
TT	$x_{ff}^2/t \times 10^{-3}$ [m²/s]	R^2	$V/t \times 10^{-7}$ [m³/s]	R^2
Test 1	4.751	0.993	13.564	0.999
Test 2	4.893	0.999	11.816	0.999
Test 3	4.472	0.999	12.068	0.999
$MEAN \pm SD$	4.705 ± 0.214		12.483 ± 0.945	

Table 11
x_{ff}^2/t, V/t and R^2 results from the permeability characterization of the AR and TT fabrics with $\Delta P = 100$ kPa.

$\Delta P = 100$ kPa	$K_{unsaturated}$		$K_{saturated}$	
AR	$x_{ff}^2/t \times 10^{-3}$ [m²/s]	R^2	$V/t \times 10^{-7}$ [m³/s]	R^2
Test 1	5.289	0.999	13.937	0.999
Test 2	5.174	0.999	14.137	0.999
Test 3	4.591	0.999	12.310	0.999
$MEAN \pm SD$	5.018 ± 0.374		13.461 ± 1.003	
TT	$x_{ff}^2/t \times 10^{-3}$ [m²/s]	R^2	$V/t \times 10^{-7}$ [m³/s]	R^2
Test 1	8.718	0.999	23.944	0.999
Test 2	8.101	0.997	21.390	0.999
Test 3	8.577	0.998	23.438	0.999
$MEAN \pm SD$	8.465 ± 0.323		22.924 ± 1.352	

Table 12
x_{ff}^2/t, V/t and R^2 results from the permeability characterization of the AR and TT fabrics with $\Delta P = -60$ kPa.

$\Delta P = -60$ kPa	$K_{unsaturated}$		$K_{saturated}$	
AR	$x_{ff}^2/t \times 10^{-3}$ [m²/s]	R^2	$V/t \times 10^{-7}$ [m³/s]	R^2
Test 1	2.913	0.999	6.208	0.999
Test 2	2.713	0.999	6.018	0.999
Test 3	2.548	0.998	5.616	0.999
$MEAN \pm SD$	2.724 ± 0.183		5.947 ± 0.302	
TT	$x_{ff}^2/t \times 10^{-3}$ [m²/s]	R^2	$V/t \times 10^{-7}$ [m³/s]	R^2
Test 1	3.695	0.999	8.132	0.999
Test 2	4.239	0.999	8.883	0.999
Test 3	3.272	0.999	7.363	0.999
$MEAN \pm SD$	3.736 ± 0.485		8.126 ± 0.760	

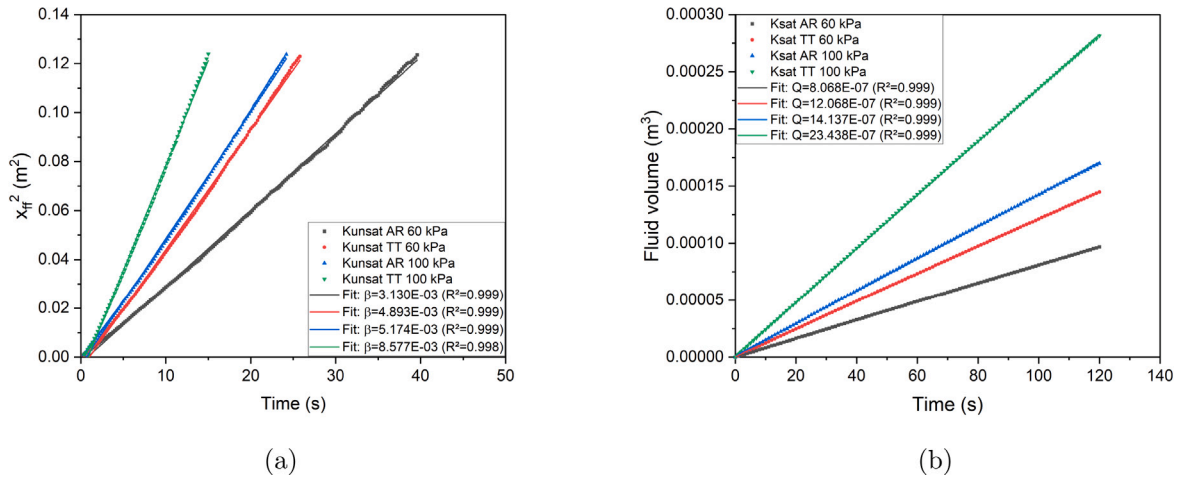

Fig. 13. Curves $x_{ff}^2 = f(t)$ (a) and $V = f(t)$ (b) for the determination of the unsaturated and saturated permeability — RTM case.

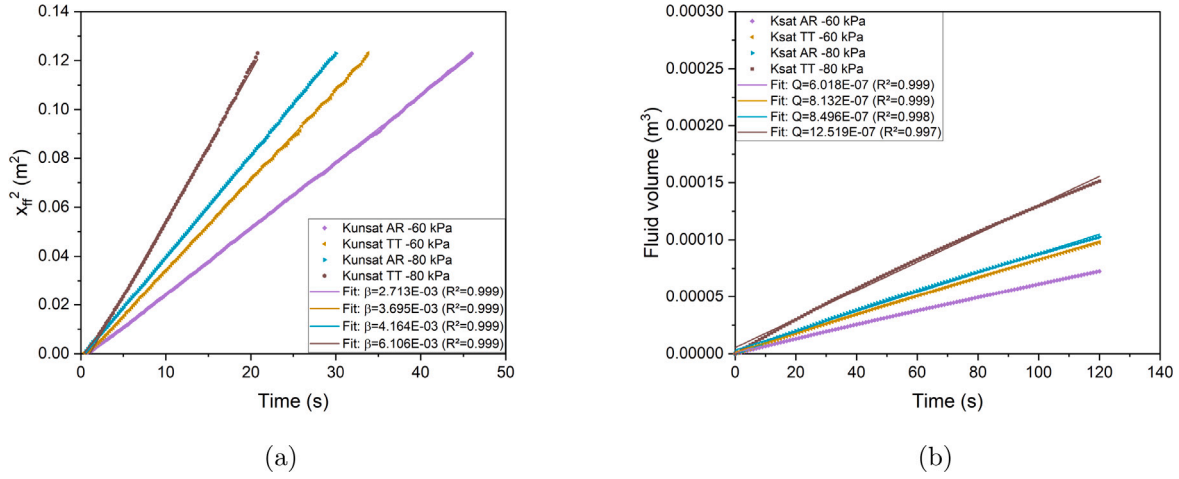

Fig. 14. Curves $x_{ff}^2 = f(t)$ (a) and $V = f(t)$ (b) for the determination of the unsaturated and saturated permeability — VARTM case.

Table 13
x_{ff}^2/t, V/t and R^2 results from the permeability characterization of the AR and TT fabrics with $\Delta P = -80$ kPa.

$\Delta P = -80$ kPa	$K_{unsaturated}$		$K_{saturated}$	
AR	$x_{ff}^2/t \times 10^{-3}$ [m²/s]	R^2	$V/t \times 10^{-7}$ [m³/s]	R^2
Test 1	4.164	0.999	8.496	0.998
Test 2	4.401	0.999	8.908	0.998
Test 3	3.998	0.999	8.015	0.998
$MEAN \pm SD$	4.188 ± 0.203		8.473 ± 0.447	
TT	$x_{ff}^2/t \times 10^{-3}$ [m²/s]	R^2	$V/t \times 10^{-7}$ [m³/s]	R^2
Test 1	6.292	0.999	13.162	0.998
Test 2	5.436	0.999	11.036	0.998
Test 3	6.106	0.999	12.519	0.997
$MEAN \pm SD$	5.945 ± 0.451		12.239 ± 1.090	

that, for a same fabric reference, K_{sat} and K_{unsat} do not depend on the pressure gradient and are equal. However, as shown in Fig. 15, K_{unsat} and K_{sat} significantly increase after thermal treatment. Theoretically, if the fabric geometry is not altered by the treatment, the K_{sat} should not vary [11]. In addition to the observation already done for the capillary wicking tests with the modification of the $c\bar{r}$ after treatment, this new result suggests that the fabric morphology could be modified after thermal treatment, in agreement with roughness results obtained by AFM. Experimentally, this tendency was also observed by Dukkipati [44]. The author highlighted that the saturated permeability tends to be higher with the unsized fiber compared to the sized fiber (with glass and carbon fibers). From a numerical point of view, Geoffre et al. [45] have carried out a study varying the fluid slip condition at the fluid/fiber interface. The authors have shown that, in the case of a non-null slip condition, the saturated permeability tends to increase compared to the case of a zero slip condition. These works tend to demonstrate that the fiber roughness modification caused by the thermal treatment could lead to a modification of the fluid slip condition at the fiber surface. This phenomena could have a significant impact on the saturated permeability of the reinforcement and could explain the tendency observed. Table 14 presents the results of the ratio R_s and its associated capillary pressure ΔP_γ, calculated according to Caglar et al. [11]. For the RTM case (60 and 100 kPa), the R_s factors are equal to 1 because of the equality between K_{sat} and K_{unsat}. The ΔP_γ associated could be considered as null due to the large scatter of these values. Consequently, in the study conditions and at the process scale, it could indicate an equilibrium between the viscous forces and the capillary effects at 60 and 100 kPa.

Fig. 16 presents the unsaturated (K_{unsat}) and saturated (K_{sat}) permeability at −60 kPa and −80 kPa for the AR and TT basalt fabrics. As for the RTM case, considering a same reference of fabric (AR or TT), the K_{sat} and K_{unsat} do not depend of the pressure gradient value. The K_{sat} is also different after thermal treatment which confirms that the thermal treatment modified the fabric morphology or the slip condition on fiber [45]. The R_s and ΔP_γ values according to Caglar et al. are

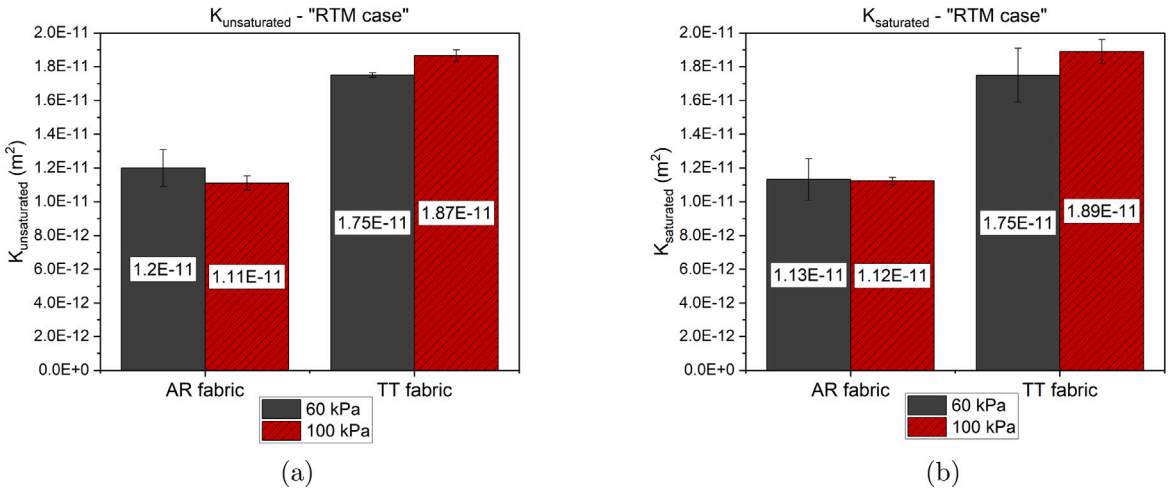

Fig. 15. Unsaturated (a) and saturated (b) permeability results — RTM case.

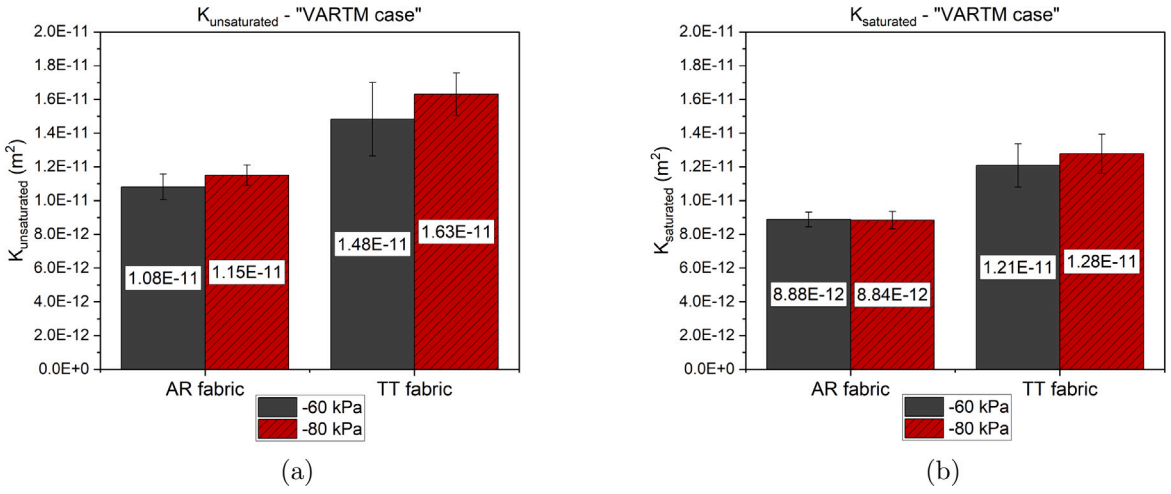

Fig. 16. Unsaturated (a) and saturated (b) permeability results — VARTM case.

presented in Table 14. The R_s factor are significantly greater than 1 which means that the K_{unsat} is greater than the K_{sat} and consequently the capillary effects would tend to dominate the flow. Moreover, the greater the pressure difference, the greater the R_s and the ΔP_γ values are. Consequently, in the study conditions, at the process scale, the capillary effects (ΔP_γ) calculated with the method from Caglar et al. [11] are not negligible compared to the applied pressure for the AR and TT basalt fabric at −60 and −80 kPa.

This estimation of capillary pressures at the process scale (Table 14) in a forced regime cannot be compared to the calculated capillary pressures (Table 9) performed with capillary wicking test in spontaneous impregnation. The considered scales, the fiber volume fraction and the impregnation regimes are different. Furthermore, the capillary pressures obtained from wicking tests cannot be used to estimate the unsaturated permeability. As detailed in Section 2.2.4, the capillary pressure value depends on the morphology of the porous medium in the sample holder. In order to do that, capillary rise should be performed with a similar fiber arrangement and volume fraction than in the permeability experiment. This will be tested in further studies and compared with numerical modeling of flows.

Table 14
R_s and ΔP_γ results from the permeability experiments with water.

Fabric reference	ΔP [kPa]	R_s	ΔP_γ [kPa] Caglar
AR	60	1.06 ± 0.04	−4.0 ± 2.5
	100	0.99 ± 0.02	1.2 ± 2.1
TT	60	1.01 ± 0.09	−0.4 ± 5.4
	100	0.99 ± 0.02	1.3 ± 2.0
AR	−60	1.22 ± 0.03	−12.4 ± 1.6
	−80	1.30 ± 0.01	−24.9 ± 1.1
TT	−60	1.22 ± 0.05	−12.7 ± 2.7
	−80	1.28 ± 0.02	−22.8 ± 1.7

4. Conclusion

This work showed the influence of the surface modification by thermal treatment of a basalt fibers on the fiber surface energy, the capillary wicking tests and the in-plane permeability experiments. The results showed that the thermal treatment increased the surface energy of the basalt fiber and particularly its polar component by 22%. The SEM and AFM analysis showed that the thermal treatment did not modify the single fiber diameter, but it affected the fiber roughness. At the mesoscopic scale, the capillary rise with water is faster after thermal treatment. It is characterized by a smaller apparent advancing contact angle and a higher equivalent capillary pressure (+68%) in a fabric roll. Results of P_{cap} obtained with different methods from literature were compared to determine the capillary pressure in spontaneous impregnation. On the other hand, the morphological factor $c\bar{r}$ varied

after thermal treatment, which could account for a morphological modification of the fabric after treatment in agreement with results at the fiber scale, probably due to a change of roughness showed with AFM. At the macroscopic scale and despite the results at lower scale, in the RTM case, the K_{unsat} and K_{sat} do not depend on the pressure gradient and are equal (R_s = 1), meaning that there could be an equilibrium between viscous forces and capillary effects. In the VARTM case, K_{unsat} and K_{sat} do not depend on the pressure gradient. It was observed that R_s is greater than 1, giving a negative ΔP_γ. It means that the capillary effects dominate the flow. However, the capillary pressure obtained with capillary wicking tests and the capillary pressure obtained form the R_S ratio cannot be compared. Finally, the saturated permeability results were different between the AR and TT fabrics in both cases of pressure gradients. Once again, this observation could be explained by a morphological modification of the fabric after thermal treatment or a roughness modification which would change the slip condition on the fiber.

The originality of this work was to highlight the fluid-fiber interaction at the microscopic and mesoscopic scales with tensiometric methods, and also to characterize the effect on the saturated and unsaturated permeability with different pressure gradients (RTM and VARTM cases) at the process scale. In first approach, the water was chosen as test liquid for its practicality (abundance and easy to clean). In a future study, this work will be carried out with other liquids having surface tension and viscosity similar to those of resins. This will allow to highlight the effect of liquid on wetting and impregnation of reinforcement as well as to be in a configuration closer to the LCM processes with resin. Moreover, carrying out permeability experiments with several pressure differences shows that the capillary pressure, calculated at the process scale in accordance with literature, can vary and become significant in the VARTM case. Further studies will be carried out to enhance the treatment method and avoid a potential modification of the fabric morphology, discriminating the effect of the roughness. Moreover investigating a lower range of pressure difference could be interesting to observe when R_s factor exceeds the unity and capillary effects are dominant. Finally, a better understanding of the phenomena involved at the front fluid area in the VARTM case is also a perspective of this study.

CRediT authorship contribution statement

Romain Ravel: Writing – review & editing, Writing – original draft, Methodology, Investigation, Conceptualization. **Monica Francesca Pucci:** Writing – review & editing, Writing – original draft, Supervision, Methodology, Investigation, Conceptualization. **Pierre-Jacques Liotier:** Writing – review & editing, Writing – original draft, Supervision, Methodology, Investigation, Conceptualization.

Declaration of competing interest

The authors declare that they have no known competing financial interests or personal relationships that could have appeared to influence the work reported in this paper.

Acknowledgments

The authors thank the mechanical workshops from Mines Saint-Etienne and IMT Mines Alès for their contribution with the manufacturing of the permeability set-up, Prof. Slangen and Mr. Lorquet for their advice for the camera and settings and finally, Mr. Chéron for his contribution in the development of the LabVIEW program for the unsaturated permeability determination.

Data availability

Data will be made available on request.

References

[1] Mangalgiri P. Composite materials for aerospace applications. Bull Mater Sci 1999;22:657–64.
[2] Kalkanis K, Psomopoulos C, Kaminaris S, Ioannidis G, Pachos P. Wind turbine blade composite materials-end of life treatment methods. Energy Procedia 2019;157:1136–43.
[3] Sozer E, Simacek P, Advani S. Resin transfer molding (RTM) in polymer matrix composites. In: Manufacturing techniques for polymer matrix composites. PMCs, Elsevier; 2012, p. 245–309.
[4] Hsiao K-T, Heider D. Vacuum assisted resin transfer molding (VARTM) in polymer matrix composites. In: Manufacturing techniques for polymer matrix composites. PMCs, Elsevier; 2012, p. 310–47.
[5] Laine B. Influence des déformations d'un renfort fibreux sur sa perméabilité: Modélisations et expériences (Ph.D. thesis), Arts et Métiers ParisTech; 2008.
[6] Mehdikhani M, Gorbatikh L, Verpoest I, Lomov SV. Voids in fiber-reinforced polymer composites: A review on their formation, characteristics, and effects on mechanical performance. J Compos Mater 2019;53(12):1579–669.
[7] Liotier P-J, Pucci MF, Le Duigou A, Kervoelen A, Tirilló J, Sarasini F, Drapier S. Role of interface formation versus fibres properties in the mechanical behaviour of bio-based composites manufactured by liquid composite molding processes. Composites B 2019;163:86–95.
[8] Park CH, Krawczak P. Unsaturated and saturated permeabilities of fiber reinforcement: critics and suggestions. Front Mater 2015;2:38.
[9] Gebart BR. Permeability of unidirectional reinforcements for RTM. J Compos Mater 1992;26(8):1100–33.
[10] Verrey J, Michaud V, Månson J-A. Dynamic capillary effects in liquid composite moulding with non-crimp fabrics. Composites A 2006;37(1):92–102.
[11] Caglar B, Tekin C, Karasu F, Michaud V. Assessment of capillary phenomena in liquid composite molding. Composites A 2019;120:73–83.
[12] Parseval YD, Pillai K, Advani SG. A simple model for the variation of permeability due to partial saturation in dual scale porous media. Transp Porous Media 1997;27:243–64.
[13] Salvatori D, Caglar B, Teixidó H, Michaud V. Permeability and capillary effects in a channel-wise non-crimp fabric. Composites A 2018;108:41–52.
[14] Alotaibi H, Jabbari M, Soutis C. A numerical analysis of resin flow in woven fabrics: Effect of local tow curvature on dual-scale permeability. Materials 2021;14(2):405.
[15] Teixidó H, Staal J, Caglar B, Michaud V. Capillary effects in fiber reinforced polymer composite processing: a review. Front Mater 2022;9:809226.
[16] Ravey C, Ruiz E, Trochu F. Determination of the optimal impregnation velocity in resin transfer molding by capillary rise experiments and infrared thermography. Compos Sci Technol 2014;99:96–102.
[17] Lundström T, Stenberg R, Bergström R, Partanen H, Birkeland P. In-plane permeability measurements: a nordic round-robin study. Composites A 2000;31(1):29–43.
[18] Arbter R, Beraud J, Binetruy C, Bizet L, Bréard J, Comas-Cardona S, Demaria C, Endruweit A, Ermanni P, Gommer F, et al. Experimental determination of the permeability of textiles: A benchmark exercise. Composites A 2011;42(9):1157–68.
[19] Vernet N, Ruiz E, Advani S, Alms JB, Aubert M, Barburski M, Barari B, Beraud JM, Berg DC, Correia N, et al. Experimental determination of the permeability of engineering textiles: Benchmark II. Composites A 2014;61:172–84.
[20] May D, Aktas A, Advani S, Berg D, Endruweit A, Fauster E, Lomov S, Long A, Mitschang P, Abaimov S, et al. In-plane permeability characterization of engineering textiles based on radial flow experiments: A benchmark exercise. Composites A 2019;121:100–14.
[21] ISO 4410:2023. Test methods for the experimental characterization of in-plane permeability of fibrous reinforcements for liquid composite moulding. Geneva, Switzerland: International Organization for Standardization; 2023.
[22] Shih C-H, Lee LJ. Effect of fiber architecture on permeability in liquid composite molding. Polym Compos 1998;19(5):626–39.
[23] Pearce N, Summerscales J. The compressibility of a reinforcement fabric. Compos Manuf 1995;6(1):15–21.
[24] Pearce NR, Summerscales J, Guild F. Improving the resin transfer moulding process for fabric-reinforced composites by modification of the fabric architecture. Composites A 2000;31(12):1433–41.
[25] Liotier P-J, Govignon Q, Swery E, Drapier S, Bickerton S. Characterisation of woven flax fibres reinforcements: Effect of the shear on the in-plane permeability. J Compos Mater 2015;49(27):3415–30.
[26] Amico S, Lekakou C. An experimental study of the permeability and capillary pressure in resin-transfer moulding. Compos Sci Technol 2001;61(13):1945–59.

[27] Garat W, Pucci MF, Leger R, Govignon Q, Berthet F, Perrin D, Ienny P, Liotier P-J. Surface energy determination of fibres for liquid composite moulding processes: Method to estimate equilibrium contact angles from static and quasi-static data. Colloids Surf A 2021;611:125787.
[28] Pucci MF, Liotier P-J, Drapier S. Capillary wicking in a fibrous reinforcement – Orthotropic issues to determine the capillary pressure components. Composites A 2015;77:133–41.
[29] Pucci MF, Seghini MC, Liotier P-J, Sarasini F, Tirilló J, Drapier S. Surface characterisation and wetting properties of single basalt fibres. Composites B 2017;109:72–81.
[30] Jeantet L, Regazzi A, Perrin D, Pucci MF, Corn S, Quantin J-C, Ienny P. Recycled carbon fiber potential for reuse in carbon fiber/PA6 composite parts. Composites B 2024;269:111100.
[31] Pawlus P, Reizer R, Wieczorowski M. Functional importance of surface texture parameters. Materials 2021;14(18):5326.
[32] ISO 25178-2:2021. Geometrical product specifications (GPS) — Surface texture: Areal — Part 2: Terms, definitions and surface texture parameters. Geneva, Switzerland: International Organization for Standarization; 2021.
[33] Francucci G, Rodríguez ES, Vázquez A. Study of saturated and unsaturated permeability in natural fiber fabrics. Composites A 2010;41(1):16–21.
[34] Michaud V. A review of non-saturated resin flow in liquid composite moulding processes. Transp Porous Media 2016;115(3):581–601.
[35] Bréard J, Henzel Y, Trochu F, Gauvin R. Analysis of dynamic flows through porous media. Part I: Comparison between saturated and unsaturated flows in fibrous reinforcements. Polym Compos 2003;24(3):391–408.
[36] Patiño-Arcila ID, Vanegas-Jaramillo JD. Modeling and simulation of filling in dual-scale fibrous reinforcements: state of the art and new methodology to quantify the sink effect. J Compos Mater 2018;52(14):1915–46.
[37] Park CH, Woo L. Modeling void formation and unsaturated flow in liquid composite molding processes: a survey and review. J Reinf Plast Compos 2011;30(11):957–77.
[38] Pillai KM. Governing equations for unsaturated flow through woven fiber mats. Part 1. Isothermal flows. Composites A 2002;33(7):1007–19.
[39] Liu H, Yu Y, Liu Y, Zhang M, Li L, Ma L, Sun Y, Wang W. A review on basalt fiber composites and their applications in clean energy sector and power grids. Polymers 2022;14(12):2376.
[40] Ahn K, Seferis J, Berg J. Simultaneous measurements of permeability and capillary pressure of thermosetting matrices in woven fabric reinforcements. Polym Compos 1991;12(3):146–52.
[41] Mortensen A, Wong T. Infiltration of fibrous preforms by a pure metal: Part III. Capillary phenomena. Metall Trans A 1990;21:2257–63.
[42] Nordlund M, Michaud V. Dynamic saturation curve measurement for resin flow in glass fibre reinforcement. Composites A 2012;43(3):333–43.
[43] Legras A, Kondor A, Heitzmann M, Truss R. Inverse gas chromatography for natural fibre characterisation: Identification of the critical parameters to determine the Brunauer–Emmett–Teller specific surface area. J Chromatogr A 2015;1425:273–9.
[44] Dukkipati RK. Experimental investigation of fiber sizing-test fluid interaction for in-plane permeability measurements of continuous fibers (Ph.D. thesis), Wichita State University; 2007.
[45] Geoffre A, Ghestin M, Moulin N, Bruchon J, Drapier S. Bounding transverse permeability of fibrous media: a statistical study from random representative volume elements with consideration of fluid slip. Int J Multiph Flow 2021;143:103751.